

ARTICLE

Received 28 Apr 2016 | Accepted 25 Oct 2016 | Published 12 Dec 2016

DOI: 10.1038/ncomms13714

OPEN

# Observation of spin Seebeck contribution to the transverse thermopower in Ni-Pt and MnBi-Au bulk nanocomposites

Stephen R. Boona<sup>1</sup>, Koen Vandaele<sup>2</sup>, Isabel N. Boona<sup>3,4</sup>, David W. McComb<sup>3,4</sup> & Joseph P. Heremans<sup>1,4,5</sup>

Transverse thermoelectric devices produce electric fields perpendicular to an incident heat flux. Classically, this process is driven by the Nernst effect in bulk solids, wherein a magnetic field generates a Lorentz force on thermally excited electrons. The spin Seebeck effect also produces magnetization-dependent transverse electric fields. It is traditionally observed in thin metallic films deposited on electrically insulating ferromagnets, but the films' high resistance limits thermoelectric conversion efficiency. Combining Nernst and spin Seebeck effect in bulk materials would enable devices with simultaneously large transverse thermopower and low electrical resistance. Here we demonstrate experimentally that this is possible in composites of conducting ferromagnets (Ni or MnBi) containing metallic nanoparticles with strong spin-orbit interactions (Pt or Au). These materials display positive shifts in transverse thermopower attributable to inverse spin Hall electric fields in the nanoparticles. This more than doubles the power output of the Ni-Pt materials, establishing proof of principle that the spin Seebeck effect persists in bulk nanocomposites.

<sup>1</sup>Department of Mechanical and Aerospace Engineering, The Ohio State University, Columbus, Ohio 43210, USA. <sup>2</sup>Department of Inorganic and Physical Chemistry, Ghent University, Ghent B-9000, Belgium. <sup>3</sup>Center for Electron Microscopy and Analysis, The Ohio State University, Columbus, Ohio 43212, USA. <sup>4</sup>Department of Materials Science and Engineering, The Ohio State University, Columbus, Ohio 43210, USA. <sup>5</sup>Department of Physics, The Ohio State University, Columbus, Ohio 43210, USA. Correspondence and requests for materials should be addressed to S.R.B. (email: boona.1@osu.edu).

The spin Seebeck effect<sup>1</sup> (SSE) offers an alternate approach to conventional thermoelectric effects for solid-state heat-to-electricity energy conversion<sup>2–5</sup>. SSE involves the injection of heat into a polarized magnetic material, resulting in a thermal spin current. This spin current is typically detected by injecting it via spin pumping<sup>6</sup> into an adjacent thin film comprising a nonmagnetic metal with strong spin-orbit interactions, such as Pt. There, the inverse spin Hall effect (ISHE)<sup>7</sup> produces a transverse electric field proportional to the polarization and density of the incident spin current. These parameters are controlled experimentally by applying a magnetic field to alter the magnetic polarization, and by adjusting the temperature drop across the structure to alter the spin current density.

The geometry of SSE structures is identical to that in which the anomalous Nernst effect (ANE) is observed, except ANE occurs entirely within single-phase conducting ferromagnets. This is why metallic ferromagnets are avoided in experiments designed to isolate and understand the physics of SSE. However, combining SSE and ANE is a useful engineering strategy for enhancing the total transverse thermopower  $S_{xyz}$  in ferromagnetic heterostructures without the need for large applied magnetic fields. Direct implementation of this concept for energy conversion means utilizing devices where the electrically active regions are thin films, leading to a different set of problems: although thin films allow for the design of devices with mechanical flexibility<sup>2</sup>, their small cross-sectional area and inherently large electrical resistance limits the maximum possible power output of such devices to the mW level at most.

Here we demonstrate that SSE and ANE can be combined in an alternate bulk geometry better suited for energy conversion. Devices based on this concept hold potential for producing power at the W to kW level, as they comprise bulk materials that can be manufactured using large-scale production processes similar to those already in use for conventional thermoelectric devices. In this geometry, the entire device volume is both electrically and thermally active, enabling significantly lower source impedance and potentially higher voltage output compared with thin-film structures. Proof of concept is demonstrated here in a Ni-Pt composite, where the addition of Pt nanoparticles results in a significant enhancement of the transverse thermopower because of combined contributions from both the Nernst effect ( $S_{\text{Nernst}}$ ) and SSE ( $S_{\text{SSE}}$ ). Together with low electrical resistivity  $\rho$ , the transverse power factor  $\text{PF}_{xyz} = S_{xyz}^2/\rho$  in the composites is increased 2–5 times compared with the reference sample, and the transverse thermoelectric figure of merit  $zT_{xyz} = T \cdot \text{PF}_{xyz}/\kappa$  ( $\kappa$  being the thermal conductivity and  $T$  the absolute temperature) increases by an order of magnitude. This result establishes that not only can SSE be observed in bulk nanocomposites, but it can also be utilized to produce significantly more electrical power from the same temperature gradient relative to single-phase magnetic materials.

## Results

**The spin Seebeck effect in thin-film structures.** A typical thin-film longitudinal SSE geometry is depicted schematically in Fig. 1a. A temperature gradient  $\nabla_x T$  is applied to a ferromagnetic insulator (FMI) possessing magnetization  $M_z$  set by applied field  $H_z$ .  $\nabla_x T$  generates a magnon flux that carries heat<sup>8</sup> and spin along  $x$ . At the surface these magnons impinge on an adjacent normal metal (NM) film whose thickness is comparable to its spin diffusion length  $l_s$ , typically 1–10 nm. This spectrally dependent<sup>9,10</sup> spin pumping action polarizes free electrons in the NM, resulting in a perpendicular electric field  $E_y$  via ISHE. The magnitude of  $E_y$  depends on the polarization and magnitude

of the injected spin current. This figure makes it apparent that from the perspective of energy conversion, electrical detection of thermally generated spin currents makes SSE functionally equivalent to a transverse thermopower.

From Fig. 1a, we define the SSE coefficient  $S_{\text{SSE}} = |E_y/\nabla_x T|_{H_z}$ . Typical values of  $S_{\text{SSE}}$  in  $\text{Y}_3\text{Fe}_5\text{O}_{12}$ (YIG)/Pt heterostructures are  $\sim 0.1 \mu\text{V K}^{-1}$  at 300 K. Recent work on  $\text{Fe}_3\text{O}_4$ /Pt multilayer thin films<sup>11</sup>, YIG/NiO/Pt heterostructures<sup>12</sup> and spin flopped antiferromagnets<sup>13</sup> show coefficients near  $6 \mu\text{V K}^{-1}$  at various temperatures. These values are much lower than the longitudinal thermopower of classical thermoelectric devices ( $200 \mu\text{V K}^{-1}$  in tetradymites<sup>14</sup>), so the intrinsic figure of merit in thin-film SSE heterostructures<sup>4,15</sup> is many orders of magnitude lower than in traditional semiconductor-based thermoelectrics.

As spin is not conserved, the spin diffusion length of spin-polarized electrons in the NM ( $l_s$ ) and magnons in the FMI ( $L_s$ ) limits the geometry, size and materials suitable for any SSE-based structures. For example, ISHE produces an electric field  $E_{\text{ISHE}}$  in the NM only if the NM thickness  $t$  is approximately equal to  $l_s$  (that is, when only 0.001 vol% or 10 p.p.m. of the total device volume is electrically active). If  $t$  is much greater than  $l_s$ , then  $E_{\text{ISHE}}$  is short circuited by electrons in the region of NM where spin current has decayed. Second,  $L_s$  limits the active thermal volume of FMI from which spin is injected into the NM. A conservative estimate for  $L_s$  in YIG at 300 K is  $10 \mu\text{m}$  (refs 16–18), although some experiments suggest a length scale of  $\sim 250 \text{ nm}$  (refs 19,20) is relevant to SSE. Regardless, this length is significantly shorter than the macroscopic sample and substrate thickness  $L$  that is typically 0.5 mm. As  $\nabla_x T$  in  $S_{\text{SSE}}$  is determined by  $\Delta T_x/L$  and not  $\Delta T_x/L_s$ , only 1% of  $\Delta T_x$  participates in generating  $E_y$ ; although thermal excitation produces larger spin current densities than resonant or electrical methods<sup>21</sup>, only a small fraction of the thermal energy is actually converted into electrical energy.

Pure SSE experiments require that the ferromagnetic material be insulating so that spin is transported only by magnons and not free electrons. Otherwise,  $E_{\text{ISHE}}$  in the NM would mix with ordinary and anomalous Nernst thermopower from the ferromagnet to give a total transverse thermopower  $S_{xyz} = S_{\text{Nernst}} + S_{\text{SSE}}$  (ref. 22). Careful separation of Nernst and SSE in bilayer structures is necessary when studying detailed origins of physical mechanisms<sup>23</sup>. For energy conversion, however, it is advantageous to combine Nernst and SSE into a single transverse thermopower, as long as both effects have the same polarity. This maximizes the voltage output per temperature gradient and enables lower electrical resistance, resulting in larger power output.

Multilayer structures are one way to accomplish this: adding additional thermally and electrically active layers<sup>11,24,25</sup> can increase  $S_{xyz}$  to  $1.8 \mu\text{V K}^{-1}$  and the extrinsic power factor  $S_{xyz}^2/R$  ( $R$  being the film sheet resistance) to  $2 \text{ pW K}^{-2}$ . Though these values can be reached at room temperature and with little to no applied magnetic field, the additional layers are still thin films. This means the electrically and thermally active regions of the device remain a small fraction of the total volume (much less than 1 vol%), and hence the devices have relatively high electrical impedance, and a significant portion of thermal energy goes unused. As an alternative approach, here we propose bulk composites as a scalable and robust way to make the entire device volume both electrically and thermally active, thus providing a viable pathway towards higher and more efficient power output.

**The SSE in bulk materials.** Figure 1b illustrates the conceptual basis for SSE in a bulk composite geometry. In general,  $E_{\text{ISHE}} = \rho \tan\theta_{\text{SH}} (\mathbf{j}_s \times \boldsymbol{\sigma})$ , where  $\rho$  and  $\theta_{\text{SH}}$  are the

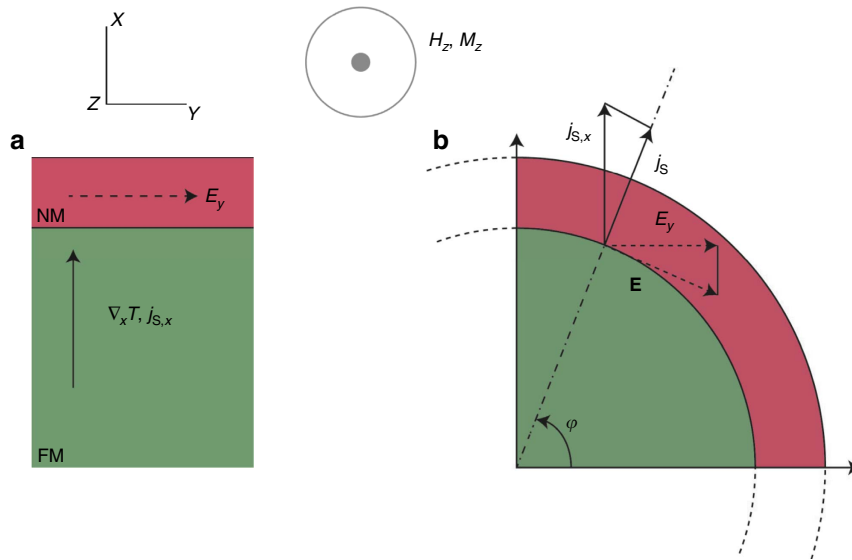


**Figure 1 | Schematic representation of the spin Seebeck effect in different geometries.** Spatial directions  $(x,y,z)$  are specified by the legend at the top. The concentric circles indicate the applied magnetic field  $H_z$  and magnetization  $M_z$  for both panels are pointing out of plane. **(a)** Geometrical layout of a conventional spin-Seebeck effect (SSE) geometry showing a normal metal (NM) film (red) on top of a ferromagnetic insulator (FMI, green). A spin current  $j_{s,x}$  is driven by a temperature gradient  $\nabla_x T$  within the FM. The polarization direction of  $j_{s,x}$  is determined by  $H_z$  and  $M_z$ . This spin current is injected into the NM, where the inverse spin Hall effect (ISHE) produces an electric field  $E_y$ . **(b)** One quadrant of the same structure folded upon itself in an FMI (green)/NM (red) core-shell configuration. Under the same conditions as **(a)** ( $H_z, M_z, \nabla_x T$ ), an ISHE field  $\mathbf{E}$  again arises in the NM, but now its directional components must be taken into account. Integrating  $\mathbf{E}$  over the full circle shows that  $E_x$  cancels out, but non-zero  $E_y$  remains (see equation (2)). This very general idea can be applied to a variety of arbitrary interface geometries, thereby providing the conceptual basis for SSE in random bulk composites.

electrical resistivity and spin Hall angle of the NM, respectively, whereas  $\mathbf{j}_s$  represents the spin current density in the NM, and  $\boldsymbol{\sigma}$  indicates the spin current polarization. Experimentally,  $\mathbf{j}_s$  is essentially proportional to  $\nabla T$ , and  $\boldsymbol{\sigma}$  is determined by the ferromagnet magnetization tensor  $\mathbf{M}$  that is set by an external applied magnetic field  $\mathbf{H}$ . As discussed above,  $\mathbf{E}_{\text{ISHE}}$  is partially short circuited by electrical conduction within the NM, resulting in attenuation that scales with  $\exp[-t/l_s]$ . Combining these and all other prefactors into a proportionality factor  $A$ , we have

$$\mathbf{E}_{\text{ISHE}} = A(\nabla T \times \mathbf{H}) \tag{1}$$

To justify the composite geometry, we consider a spherical FMI particle coated with a NM film (Fig. 1b). When subjected to  $\mathbf{H} = (0,0,H_z)$  and  $\nabla T = (\nabla_x T, 0, 0)$ , equation 1 indicates  $\mathbf{E}_{\text{ISHE}}$  develops tangentially to the NM/FMI interface in the  $(x,y)$  plane. Integrating  $\mathbf{E}_{\text{ISHE}}$  over the entire sphere reveals  $E_x = 0$  whereas  $E_y(\varphi) = A|\nabla T||\mathbf{H}|\sin^2\varphi$ , such that  $E_y \geq 0$  for all  $\varphi$ . Assuming the sphere's radius  $r \gg t$ , then  $S_{xyz}$  becomes:

$$E_y/\nabla_x T = A|\mathbf{H}| \int_0^{2\pi} \sin^2\varphi d\varphi = \pi A|\mathbf{H}| \tag{2}$$

Equation (2) gives a value of  $E_y$  that is one-half that of a slab with the same length as the periphery of the sphere. Admittedly, attenuation of  $\mathbf{E}_{\text{ISHE}}$  via short circuit through the NM is slightly enhanced in this spherical geometry over the traditional planar geometry, but we numerically estimate this factor to be  $\sim 15\%$  for  $t \approx l_s$ .

By equation (2), we propose that any bulk composite material comprising an FMI surrounded by a percolated network of sufficiently small NM grains should display a prominent  $S_{xyz} = S_{\text{SSE}}$ . Yet, this geometry is not the most favourable option for demonstrating such an effect, for two reasons. First, this approach requires compaction and sintering of FMI particles coated with thin shells of NM material. This presents processing difficulties, as a percolated nanoscale conducting pathway of NM

grains must be maintained after sintering to observe SSE and extract electrical current. Second, spin transfer from FMIs into NMs depends on the FMI/NM interface quality<sup>26</sup> that is difficult to control in bulk materials.

We address both issues through the inverted geometry, wherein NM nanoparticles (NMNPs) are embedded within a ferromagnetic conductor (FMC) matrix. By the same logic described above, individual NMNPs in contact with FMC grains will display within them nonzero  $\mathbf{E}_{\text{ISHE}}$ , so long as the depth of NMNPs along  $x$  is comparable to  $l_s$ . Current can then be extracted through the FMC matrix, and  $\mathbf{E}_{\text{ISHE}}$  in the NMNP ( $S_{\text{SSE}}$ ) will be superimposed on the background Nernst signal of the FMC ( $S_{\text{Nernst}}$ ), as in ref. 22. This approach circumvents the need for a percolated conducting path of NM, enables the NMNPs to add their  $\mathbf{E}_{\text{ISHE}}$  to the transverse voltage (if the polarities are chosen right) and simultaneously decreases the voltage source impedance. The latter effects both improve power efficiency.

This approach furthermore enables improved interfacial spin transfer efficiency, as spin currents entering the NMNPs arise from both magnons and spin-polarized electrons. However, the magnitude of  $\mathbf{E}_{\text{ISHE}}$  is still limited by the degree of spin polarization in the FMC and the frequency of electronic spin-flip scattering at the FMC/NM boundaries. The sign of  $\mathbf{E}_{\text{ISHE}}$  within the NM depends on the sign of  $\theta_{\text{SH}}$  and the relative orientations of  $\nabla T$  and  $\mathbf{M}$ , and hence we nominally expect the  $S_{\text{SSE}}$  polarity to be independent of  $S_{\text{Nernst}}$ . In addition, the electrical conductances of the FMC and the NM must be impedance matched to have the appropriate additive effect on the ISHE and Nernst voltages that are electrically connected like voltage sources in parallel; that is, the FMC cannot have high electrical conductance.

**Experimental results.** Details of the synthesis, measurement, characterization and data analysis are provided in the Methods and Supplementary Information.

We synthesized five samples, summarized in Table 1. The first sample consisted of pure polycrystalline Ni nanoparticles (NiNP) produced via precipitation reaction. This sample was used to establish a baseline for  $S_{\text{Nernst}}$  in the matrix material. Two other samples were NiNP-PtNP composites made via coprecipitation from solution of Ni and 2 wt% Pt. The fourth and fifth samples were made with MnBi as the host material and Au nanoparticles (AuNP) as the embedded NM phase.

In order to mitigate agglomeration of the PtNP and prevent possible alloying of Ni with Pt, the Ni-based composite samples were sintered at 250 °C, well below the melting point of the constituent phases. This resulted in samples that were mechanically stable but only ~50% dense, with no lattice parameter shifts or other signs of alloying (see Supplementary Fig. 1 and Supplementary Notes).

Figure 2a shows a representative electron micrograph of a composite sample obtained after sintering. From this image, we see that the sample consists of Ni particles ~100 nm in diameter and partially coated in a thin layer of NiO ~5 nm thick. These Ni particles also appear to be decorated with small Pt nanoparticles ~5 nm in size (see Supplementary Figs 2 and 3 and Supplementary Notes for additional images). The PtNP sometimes form larger agglomerates nearly 20 nm in size, as seen in parts of the image. These particles, including the agglomerates, are well within the size range where we expect an appreciable ISHE field to arise within the Pt because of thermal spin injection from the adjacent Ni.

The thin layer of NiO observed at the edges of the Ni grains implies that the transport properties of the samples we report here are likely much different from those of pure, dense, bulk Ni. This emphasizes the importance of utilizing a reference sample prepared in the same manner as the composites. As it remains unclear how many interfaces in the sample are Ni/Pt and how many are Ni/NiO/Pt, we must consider what happens in the latter case. The presence of thin layers of electrically insulating NiO is certain to affect charge and spin transport between the Ni and Pt particles. However, as NiO is antiferromagnetic, spin currents can still propagate through thin layers of this material; this has been demonstrated in several recent studies, one of which observed spin currents transmitted through NiO layers up to 100 nm thick in  $\text{Y}_3\text{Fe}_5\text{O}_{12}/\text{NiO}/\text{Pt}$  heterostructures, as well as multiple studies that suggest the addition of NiO actually enhances the transmission of spin currents under certain conditions<sup>12,27–29</sup>. The presence of NiO undoubtedly has a detrimental effect on the electrical resistivity and power factor of both the reference and composite materials, although we anticipate these effects may be partially negated by a corresponding decrease in thermal conductivity.

With this in mind, we examine the transverse thermopower data collected at 125 K and shown in Fig. 2b for the NiNP reference and NiNP-PtNP(1). The inset shows the difference in

thermopower between the two samples overlaid with the NiNP magnetization at the same temperature. From the main figure, we see that the slopes of the transverse thermopowers versus field are approximately equal at fields > 0.5 T, where the magnetization is saturated (the ordinary Nernst effect (ONE)), whereas they are significantly different at fields < 0.5 T, where the magnetization is changing (the ANE). The difference between the thermopowers of the two materials tracks the NiNP magnetization, consistent with the hypothesis that an ISHE field arises within the PtNP. We note that essentially no hysteresis was observed in the thermopower, and very minimal hysteresis was detected in the NiNP magnetization.

The ANE coefficients  $[E_y/\nabla_x T]/H_z$  (that is, low-field thermopower slopes) for each of the NiNP-based samples are plotted versus temperature in Fig. 2c. At every temperature, the samples containing PtNP have larger ANE coefficients than the sample without, indicating an additional magnetization-dependent contribution to the thermopower. A plot of the high-field ONE coefficients versus temperature is included in Supplementary Fig. 4. We do not observe any appreciable difference in ONE coefficient among the three samples, indicating that the addition of a few wt% PtNP has no significant or systematic effect on the transverse thermopower when the magnetization is saturated.

The electrical resistivity of all three samples is shown in Fig. 2d. The samples containing PtNP are very similar to one another and slightly more resistive than the reference sample that is ~10 times more resistive than dense Ni. The resistivity and ANE data are combined in Fig. 2e, where we plot the intrinsic transverse power factor  $\text{PF}_{xyz} = (S_{xyz})^2/\rho$  at various temperatures for all three samples. As there is essentially no remnant magnetization in these materials,  $\text{PF}_{xyz}$  was calculated using the transverse thermopower at  $H_z = 0.1$  T, an applied magnetic field easily reached with permanent magnets. These data show that the addition of PtNP increases  $\text{PF}_{xyz}$  between 2 and 5 times compared with the matrix material alone. Thermal conductivity ( $\kappa$ ) data are also presented in Fig. 2f. Nanostructuring dominates  $\kappa$  in these samples, as indicated by the relatively low magnitude and extremely flat temperature dependence. Like  $\rho$ ,  $\kappa$  is reduced by ~20% between the NiNP and the NiNP-PtNP sample 1; however, the variation in  $\kappa$  between the two Pt-containing samples is larger than the corresponding change in  $\rho$ , presumably because of variations in microstructure resulting from slight differences in processing conditions.

These data can be combined to calculate a transverse thermoelectric figure of merit  $zT_{xyz} = T \cdot \text{PF}_{xyz}/\kappa$ , where  $T$  is the absolute temperature. The transverse  $zT_{xyz}$  values (not shown) follow the trend in  $\text{PF}_{xyz}$  amplified by their variation in  $\kappa$ . The  $zT_{xyz}$  values remain small, as they are in all conventional metals and SSE structures. Regardless, we observe an order of magnitude increase in  $zT_{xyz}$  at 100 K between the composite and reference samples, a dramatic improvement that can be attributed entirely to the spin Seebeck effect.

To provide a further check on the composite concept, we examined two additional samples where the host material (MnBi) has an ANE coefficient with polarity opposite to that of Ni, but the NMNPs (Au) still have positive spin Hall angles. Au was used instead of Pt because it has a much longer spin diffusion length, allowing for relatively large Au particles (above 50 nm) to be present without completely short circuiting the ISHE electric field. The wet chemistry used to prepare Ni and Pt NP's cannot be applied in this case because MnBi is moisture sensitive, and hence a different approach was utilized (see Methods).

The transverse thermopower of pure MnBi and a MnBi-AuNP composite at 300 K are depicted in Fig. 3. To our knowledge, these are the first published data of the thermomagnetic properties of MnBi. The presence of AuNP in the composite

**Table 1 | Summary of the samples studied here.**

Sample name	Host compound	Nanoparticles	NP size (nm)	ANE of host*	$\theta_{SH}$ of NP
NiNP	Ni	Ni	100	+	N/A
NiNP-PtNP(1)	Ni	Ni + Pt	100 (Ni), 5 (Pt)	+	+
NiNP-PtNP(2)	Ni	Ni + Pt	100 (Ni), 5 (Pt)	+	+
MnBi	MnBi	N/A	N/A	–	N/A
MnBi-AuNP	MnBi	Au	50 nm	–	+

\*Based on the spin Seebeck sign convention that is opposite to that of Gerlach.

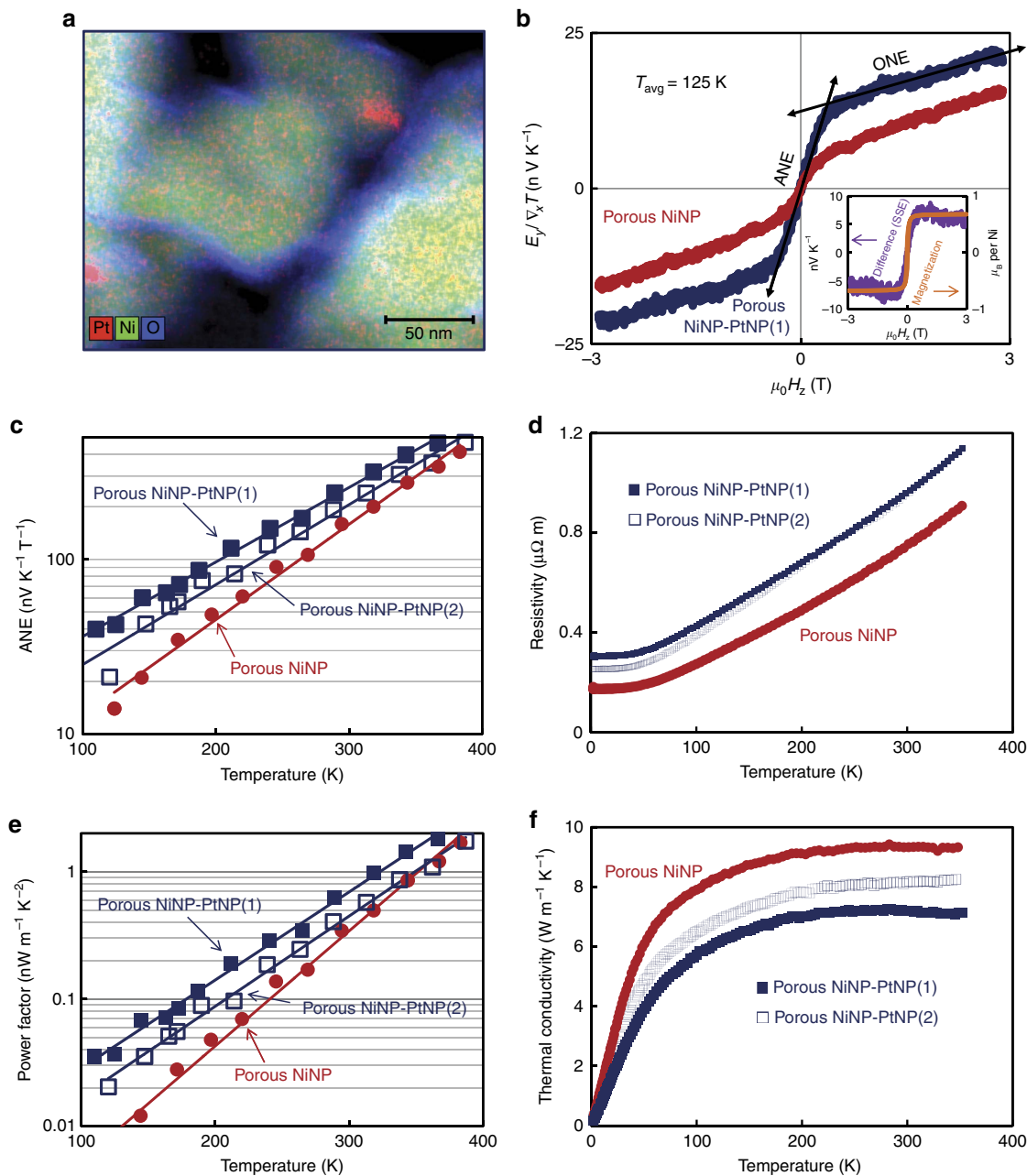


**Figure 2 | Microstructure and transport properties of Ni-Pt composites.** (a) High-angle annular dark-field (HAADF) image of NiNP-PtNP(2) overlaid with false-colour elemental mapping of Pt (red), Ni (green) and O (blue) determined by X-ray energy-dispersive spectroscopy (XEDS) in a scanning transmission electron microscope (STEM). (b) Transverse thermopower versus applied field at 125 K for porous NiNP (red) and porous NiNP-PtNP(1) (blue). The slopes at low and high fields give the ANE and ONE coefficients, respectively. The inset shows the difference between the red and blue curves (purple), along with the sample magnetization (orange). (c) ANE coefficients of the three samples versus temperature. Solid lines are a guide for the eye. (d) Resistivity of all three samples versus temperature. (e) Temperature dependence of the intrinsic power factor of NiNP (red circles), NiNP-PtNP(1) (solid blue squares) and NiNP-PtNP(2) (empty blue squares) at  $H_z = 0.1$  T. Solid lines are a guide for the eye. (f) Thermal conductivity of all three samples versus temperature.

shifts  $E_y/\nabla_x T$  towards a more positive value, consistent with positive  $\theta_{\text{SH}}$  in Au, and therefore with the existence of an ISHE contribution from the AuNP. The difference between the transverse thermopowers of the two materials is plotted in the lower left inset, along with the magnetization of MnBi powder.

Admittedly, any shift in transverse thermopower where the magnitude decreases is difficult to uniquely attribute to an ISHE field in the NMNP, as this may also result from simpler mechanisms like short circuits of the ANE electric field across larger NM particles. However, in this case, we observe the

difference curve follows the same general field dependence of the magnetization, including a small hysteresis loop (upper right inset of Fig. 3), indicating that the shift in thermopower is not simply a constant offset arising from a short circuit of the ANE field. The size of this hysteresis loop is not particularly meaningful, as (unlike thin-film samples) we do not expect the ISHE field to follow exactly the hysteresis loop of the entire sample; instead, the ISHE hysteresis loop should reflect the magnetization of individual MnBi particles from which spin currents are thermally injected into neighbouring AuNP. The absolute magnitude of the

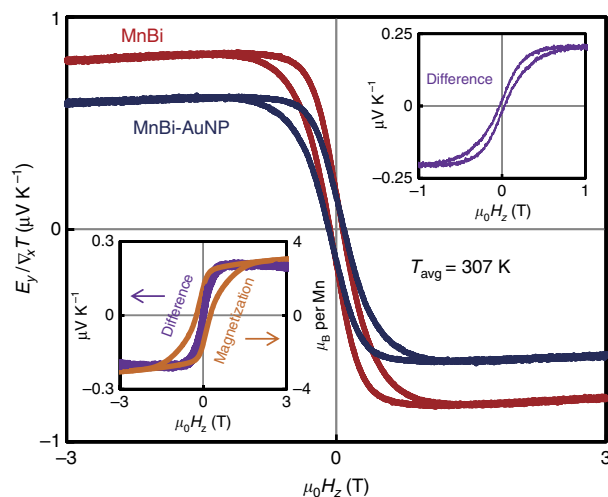


**Figure 3 | Transverse thermopower of MnBi-Au composites at 307 K.** The red trace indicates the thermopower of MnBi, whereas that of MnBi-AuNP is shown in blue. The lower left inset shows the difference between these curves (purple) as well as the magnetization of the MnBi at 307 K (orange), whereas the upper right inset emphasizes the hysteresis loop in the difference plot.

difference (the SSE voltage) appears to be significantly larger in this sample than it is in the Ni-Pt composites, although the relative change compared with the reference sample is similar. This is probably a reflection of differences in the ratio of electrical resistivity between the FMC and NM phases; Pt and Ni are roughly within a factor of two of each other, whereas our MnBi sample is at least an order of magnitude more resistive than Au (see Supplementary Fig. 5). In this regard, the FMC matrix phase is less likely to short circuit the SSE voltage in MnBi-AuNP than in NiNP-PtNP, leading to larger  $S_{SSE}$ .

## Discussion

Put together, these data demonstrate that the SSE can be observed and exploited not only in thin-film structures, but now also in bulk composite materials. Though we discuss our results above in terms of the conventional thermoelectric power factor concept, which we parse into intrinsic and extrinsic when comparing composites with thin films, it is perhaps more intuitive to simply consider the total power output of hypothetical devices based on each concept. As bulk composites allow for electrical power to be extracted through their entire volume and thus provide far less internal resistance than thin films, such devices would be capable of producing significantly more total power from the same temperature gradient.

Broadly speaking, the composite concept applies to a wide variety of material combinations, and it invites further experimental and theoretical optimization of spin transport and spin pumping in irregular and/or random geometries. Further developments in materials selection and processing may lead to substantial increases in thermoelectric performance of magnetic composites beyond the order of magnitude improvement we report here, including large remnant transverse thermopowers that can produce voltage even in the absence of applied magnetic fields. If so, this approach may enable the development of low-cost SSE-based devices that require no vacuum processing and have dimensions like those of conventional thermoelectric materials, providing access to high power thermal energy conversion applications.

## Methods

**Material synthesis.** All samples used for transport property measurements were polycrystals compacted from powders by spark plasma sintering into 10 mm diameter cylindrical pellets  $\sim 1$ –2 mm thick. The nanoparticles used in this study were either Au (AuNP), which had diameters before sintering of  $\sim 50$  nm and were purchased commercially (Sigma Aldrich), or Pt (PtNP), which had diameters before sintering of 2–5 nm and were chemically and mechanically dispersed among Ni nanoparticles during synthesis at the Ohio State University.

PtNP and NiNP were synthesized by reducing  $\text{Ni}(\text{NO}_3)_2 \cdot 6\text{H}_2\text{O}$  with  $\text{NaBH}_4$  in the presence of  $\text{H}_2\text{PtCl}_6 \cdot 6\text{H}_2\text{O}$  and sodium citrate as complexing agent. The resulting NiNP were amorphous (a-NiNP) and intimately mixed with PtNP, as observed by imaging in the scanning transmission electron microscope (STEM). The a-NiNP was then converted to crystalline NiNP by post reduction treatment with  $\text{N}_2\text{H}_4 \cdot \text{H}_2\text{O}$ . Hydrogen hexachloroplatinate(IV) hydrate, ca. 40% Pt, and sodium borohydride powder 99% were purchased from Acros Organics. Sodium citrate dihydrate >99%, nickel nitrate hexahydrate 99.99%, 64–65% hydrazine monohydrate and 99.8% ethylene glycol were supplied by Sigma Aldrich. All chemicals were used as received.

In a typical synthesis, 4 g  $\text{Ni}(\text{NO}_3)_2 \cdot 6\text{H}_2\text{O}$  salt and 0.0428 g  $\text{H}_2\text{PtCl}_6 \cdot 6\text{H}_2\text{O}$  were dissolved in 250 ml water and stabilized by 8.77 g sodium citrate. Subsequently, the solution was heated to 80 °C and 1.56 g  $\text{NaBH}_4$  was dissolved in 20 ml water. Then, 7.15 g NaOH was added and the mixture was stirred vigorously for 15 min. Next, 10.8 ml  $\text{N}_2\text{H}_4 \cdot \text{H}_2\text{O}$  in 20 ml ethyleneglycol was added to the solution and stirred for 1 h at 80 °C. The nanocomposite powder was collected magnetically and washed thoroughly with water and ethanol. The dried powder was then compacted by spark plasma sintering under 50 MPa of uniaxial pressure at 250 °C held for 30 min in a graphite die under continuous vacuum.

Polycrystalline powders of MnBi were synthesized through a combination of arc melting, grinding, sieving and annealing, using the methods similar to those described in ref. 30. The MnBi-AuNP composite sample was created by mixing 5 vol% AuNP with 95 vol% MnBi powder ( $\sim 125$  mesh) and sonicating in a hexane bath at 35 kHz for 20 min. As MnBi is moderately air and water sensitive, hexane was used to prevent decomposition. The suspension was dried then sintered under 50 MPa of uniaxial pressure at a temperature of 200 °C held for 5 min in a graphite die under continuous vacuum. The control sample of MnBi was synthesized from the same batch of powder under the same conditions but without AuNP.

**Structural and compositional characterization.** X-ray diffraction analysis was performed using a Rigaku MiniFlex Diffractometer with Cu-K $\alpha$  radiation. Based on the X-ray diffraction results, we successfully synthesized high-purity polycrystalline MnBi and MnBi-AuNP materials containing no discernible impurity phases (see Supplementary Fig. 6 and Supplementary Notes). We also observe no discernible peak shift in the Ni-Pt composites, indicating no alloying occurred between Ni and Pt during sintering at 250 °C.

Microstructural analysis was performed on several samples of control and composite materials by scanning electron microscopy (SEM) and STEM with high-angle annular dark-field (HAADF) imaging and X-ray energy-dispersive spectroscopy (XEDS). The HAADF-STEM imaging and XEDS spectrum collection was performed using a monochromated FEI Titan 60-300 STEM equipped with a Super-X XEDS collection system. The SEM work and XEDS spectra were collected using the FEI Sirion field emission SEM equipped with the EDAX Octane Super SDD system.

SEM analysis of the AuNP shows Au inclusions ranging in size from  $\sim 50$  nm particles up to 20  $\mu\text{m}$  agglomerates. STEM and XEDS analysis of the NiNP-PtNP before sintering indicated 2–5 nm PtNP. After sintering, we observed various nanostructured features that included 20 nm Pt agglomerates and what appear to be PtNP under 5 nm in diameter widely dispersed and decorating the Ni grains. Additional representative images are provided in the Supplementary Information.

**Measurements.** Parallelepiped pieces of each sample were cut using a rotary diamond saw. Silver epoxy (EpoTech) was used as a conducting adhesive to attach gold-coated copper leads, heat spreaders and heat sinks to the samples in a five-probe configuration. All transport measurements were performed in a Quantum Design Physical Property Measurement System via the Thermal Transport Option. Transverse thermopower measurements were performed using the five-probe technique with a home-built breakout box, whereas electrical resistivity was measured using a conventional AC four-probe method. Seebeck coefficient and thermal conductivity were determined using a continuous measurement protocol.

For transverse thermopower measurements, a steady-state temperature difference  $\Delta T_x$  was established and then the corresponding transverse voltage  $\Delta V_y$  was recorded while continuously sweeping the applied magnetic field  $H_z$  back and forth between maximum and minimum values of  $H_z = 30$  kOe at a constant rate of 50 Oe  $\text{s}^{-1}$ . The data were analyzed by averaging out the odd components to isolate the hysteresis curve for each temperature point. These signals were then normalized by the corresponding field-dependent temperature difference as well as by the associated lengths in order to arrive at the intrinsic  $S_{xyz}$  coefficient.

**Data availability.** The data that support the findings of this study are available from the corresponding author upon request.

## References

- Uchida, K. *et al.* Observation of longitudinal spin-Seebeck effect in magnetic insulators. *Appl. Phys. Lett.* **97**, 172505 (2010).
- Kirihara, A. *et al.* Spin-current-driven thermoelectric coating. *Nat. Mater.* **11**, 686 (2012).
- Boona, S. R., Myers, R. C. & Heremans, J. P. Spin caloritronics. *Energ. Environ. Sci.* **7**, 885–910 (2014).
- Uchida, K. *et al.* Thermoelectric generation based on spin Seebeck effects. *P. IEEE* **104**, 1946–1973 (2016).
- Boona, S. R., Watzman, S. J. & Heremans, J. P. Research update: utilizing magnetization dynamics in solid-state thermal energy conversion. *APL Mater.* **4**, 104502 (2016).
- Tserkovnyak, Y., Brataas, A. & Bauer, G. E. W. Spin pumping and magnetization dynamics in metallic multilayers. *Phys. Rev. B* **66**, 224403 (2002).
- Saitoh, E., Ueda, M., Miyajima, H. & Tatara, G. Conversion of spin current into charge current at room temperature: inverse spin-Hall effect. *Appl. Phys. Lett.* **88**, 182509 (2006).
- Boona, S. R. & Heremans, J. P. Magnon thermal mean free path in yttrium iron garnet. *Phys. Rev. B* **90**, 064421 (2014).
- Jin, H., Boona, S. R., Yang, Z., Myers, R. C. & Heremans, J. P. Effect of the magnon dispersion on the longitudinal spin Seebeck effect in yttrium iron garnets. *Phys. Rev. B* **92**, 054436 (2015).
- Geprags, S. *et al.* Origin of the spin Seebeck effect in compensated ferromagnets. *Nat. Comm.* **7**, 10452 (2015).
- Ramos, R. *et al.* Unconventional scaling and significant enhancement of the spin Seebeck effect in multilayers. *Phys. Rev. B* **92**, 220407(R) (2015).
- Lin, W., Chen, K., Zhang, S. & Chien, C. L. Enhancement of thermally injected spin current through an antiferromagnetic insulator. *Phys. Rev. Lett.* **116**, 186601 (2016).
- Wu, S. M. *et al.* Antiferromagnetic spin Seebeck effect. *Phys. Rev. Lett.* **116**, 097204 (2016).
- Heremans, J. P. & Wiendlocha, B. in *CRC Handbook on Thermoelectrics* (ed. Uher, C.) Ch. 2 (Taylor and Francis, 2016).
- Cahaya, A. B., Tretiakov, O. A. & Bauer, G. E. W. Spin Seebeck power generators. *Appl. Phys. Lett.* **104**(4): 042402 (2014).
- Cornelissen, L. J., Liu, J., Duine, R. A., Ben Youssef, J. & van Wees, B. J. Long-distance transport of magnon spin information in a magnetic insulator and room temperature. *Nat. Phys.* **11**, 1022 (2015).
- Rezende, S. M. *et al.* Magnon spin-current theory for the longitudinal spin-Seebeck effect. *Phys. Rev. B* **89**, 014416 (2014).
- Giles, B. L., Yang, Z., Jamison, J. S. & Myers, R. C. Long-range pure magnon spin diffusion observed in a nonlocal spin-Seebeck geometry. *Phys. Rev. B* **92**, 224415 (2015).
- Kehlberger, A. *et al.* Length scale of the spin Seebeck effect. *Phys. Rev. Lett.* **115**, 096602 (2015).
- Wu, H. *et al.* Observation of magnon-mediated electric current drag at room temperature. *Phys. Rev. B* **93**, 060403(R) (2016).
- Weiler, M. *et al.* Experimental test of the spin mixing interface conductivity concept. *Phys. Rev. Lett.* **111**, 176601 (2013).
- Ramos, R. *et al.* Observation of the spin Seebeck effect in epitaxial Fe<sub>3</sub>O<sub>4</sub> thin films. *Appl. Phys. Lett.* **102**, 072413 (2013).
- Kikkawa, T. *et al.* Longitudinal spin Seebeck effect free from the proximity Nernst effect. *Phys. Rev. Lett.* **110**, 067207 (2013).
- Lee, K.-D. *et al.* Thermoelectric signal enhancement by reconciling the spin Seebeck and anomalous Nernst effects in ferromagnet/non-magnet multilayers. *Sci. Rep.* **5**, 10249 (2015).
- Ramos, R. *et al.* Thermoelectric performance of spin Seebeck effect in Fe<sub>3</sub>O<sub>4</sub>/Pt-based thin film heterostructures. *APL Mater.* **4**, 104802 (2016).
- Kehlberger, A. *et al.* Investigation of the magnetic properties of insulating thin films using the longitudinal spin Seebeck effect. *J. Appl. Phys.* **115**, 17C731 (2014).
- Wang, H., Du, C., Hammel, P. C. & Yang, F. Antiferromagnon spin transport from Y<sub>3</sub>Fe<sub>5</sub>O<sub>12</sub> into NiO. *Phys. Rev. Lett.* **113**, 097202 (2014).
- Shang, T. *et al.* Effect of NiO inserted layer on spin-Hall magnetoresistance in Pt/NiO/YIG heterostructures. *Appl. Phys. Lett.* **109**, 032410 (2016).
- Prakash, A., Brangham, J., Yang, F. & Heremans, J. P. Spin Seebeck effect through antiferromagnetic NiO. *Phys. Rev. B* **94**, 014427 (2016).
- Choi, J. P., Lavender, C. A., Li, G. & Cui, J. Process for preparing scalable quantities of high purity manganese bismuth magnetic materials for fabrication of permanent magnets, US Patent 14/059,773 (2015).

## Acknowledgements

This work is supported by the US National Science Foundation MRSEC program under Grant No. DMR1420451 and by the US Army Research Office MURI program under Grant No. W911NF-14-1-0016. Microscopy was performed at The Ohio State University (OSU) Center for Electron Microscopy and Analysis (CEMAS).

## Author contributions

S.R.B. devised the study with feedback and supervision from J.P.H., who also derived the model equations. S.R.B. also synthesized the MnBi powder, sintered the pellets, performed the transport and X-ray diffraction (XRD) measurements and conducted the data analysis. K.V. performed the wet chemistry, including synthesis of the Ni-PtNP powders. I.N.B. performed all microscopy analyses with feedback and supervision from D.W.M. All authors contributed to writing and editing the manuscript and supplement.

## Additional information

**Supplementary Information** accompanies this paper at <http://www.nature.com/naturecommunications>

**Competing financial interests:** The authors declare no competing financial interests.

**Reprints and permission** information is available online at <http://npg.nature.com/reprintsandpermissions/>

**How to cite this article:** Boona, S. R. *et al.* Observation of spin Seebeck contribution to the transverse thermopower in Ni-Pt and MnBi-Au bulk nanocomposites. *Nat. Commun.* **7**: 13714 doi: 10.1038/ncomms13714 (2016).

**Publisher's note:** Springer Nature remains neutral with regard to jurisdictional claims in published maps and institutional affiliations.



This work is licensed under a Creative Commons Attribution 4.0 International License. The images or other third party material in this article are included in the article's Creative Commons license, unless indicated otherwise in the credit line; if the material is not included under the Creative Commons license, users will need to obtain permission from the license holder to reproduce the material. To view a copy of this license, visit <http://creativecommons.org/licenses/by/4.0/>

© The Author(s) 2016